THE SPECTRAL ICE CHAMBER: APPLICATION TO TITAN'S STRATOSPHERIC ICE CLOUDS

C.M. Anderson,[1] D. Nna-Mvondo,[1,2] R.E. Samuelson,[1,3] J.L. McLain,[1,3] and J.P. Dworkin[1]

[1] NASA Goddard Space Flight Center
8800 Greenbelt Road, MC 691
Greenbelt, MD 20771, USA
[2] University Space Research Association
7178 Columbia Gateway Drive
Columbia, MD 21046, USA
[3] University of Maryland College Park
Department of Astronomy, 4296 Stadium Dr.
College Park, MD 20742-2421, USA

ABSTRACT

An ice chamber for obtaining thin-film transmission spectra of Titan-relevant organic ices between 50 and 11,700 cm^{-1} (200 to 0.85 μm) is described in detail in this work. The ice chamber, called the SPECtroscopy of Titan-Related ice AnaLogs (SPECTRAL) chamber, is located in the Spectroscopy for Planetary ICes Environments (SPICE) laboratory at NASA Goddard Space Flight Center (GSFC). Organic vapors are typically deposited between 30 K and 150 K via a variable leak valve onto a chemical vapor deposition (CVD) diamond substrate, where condensation directly into the solid state occurs. Quantitative thin-film infrared transmission spectra of the given ice or ice mixture are then measured, from which optical constants (complex indices of refraction) are computed. These optical constants in turn provide the necessary input for interpreting radiative transfer analyses of Cassini's Composite InfraRed Spectrometer (CIRS) observations of Titan's organic stratospheric ice clouds to determine their chemical compositions, abundances, and vertical distributions as functions of Titan latitude and season.

Corresponding author: C.M Anderson
carrie.m.anderson@nasa.gov

1. INTRODUCTION

During the Voyager 1 flyby of Titan in November 1980, the InfraRed Interferometer Spectrometer (IRIS) revealed Titan's stratosphere to contain a plethora of organic vapors (see for example Hanel et al. 1981; Maguire et al. 1981; Coustenis et al. 1999). The abundance of these vapors suggested that condensation directly from the vapor to solid phase should be occurring to form ice clouds in Titan's cold lower stratosphere (*e.g.,* Maguire et al. 1981; Sagan & Thompson 1984; Frere et al. 1990; Samuelson et al. 1997; Coustenis et al. 1999; Raulin & Owen 2002). Included are the hydrocarbon ices of ethane (C_2H_6), acetylene (C_2H_2), diacetylene (C_4H_2), methylacetylene (C_3H_4), propane (C_3H_8), and benzene (C_6H_6), as well as the nitrile ices of hydrogen cyanide (HCN), cyanoacetylene (HC_3N), cyanogen (C_2N_2), and dicyanoacetylene (C_4N_2).

More than two decades following the Voyager missions, the Cassini spacecraft entered into Saturn orbit in 2004. Over Cassini's 13-year mission tenure, the Composite InfraRed Spectrometer (CIRS) – the successor to IRIS – observed numerous ice clouds of varying chemical compositions in Titan's winter polar stratospheres (see Samuelson et al. 2007; de Kok et al. 2007; Anderson et al. 2010; Anderson & Samuelson 2011; Jennings et al. 2012a,b; Anderson et al. 2014, 2016; Vinatier et al. 2018). In order to identify and quantify these observed ice cloud spectral features, laboratory transmission spectra of thin ice films, leading to derived optical constants for the ices, are essential. This paper details the SPECtroscopy of Titan-Related ice AnaLogs (SPECTRAL) chamber located in the Spectroscopy for Planetary ICes Environments (SPICE) Laboratory at NASA Goddard Space Flight Center (GSFC). Although the SPECTRAL chamber is mostly focused on Titan stratospheric ice studies, its capabilities are also applicable to a much broader range of planetary objects such as gas and ice giant planet atmospheres, relatively cool exoplanet atmospheres, icy surfaces and atmospheres of Kuiper belt objects, icy moon surfaces, plume jet particulates, asteroid icy surfaces, and comets.

Formerly, transmission spectroscopy measurements and optical constant calculations of Titan's stratospheric ice analogs were determined strictly from annealing procedures (see for example Khanna et al. 1988; Masterson & Khanna 1990; Dello Russo & Khanna 1996; Khanna 2005; Moore et al. 2010). In this approach, the organic vapor is deposited at a cold temperature, typically around 30 K, in order to restrict the ice to its amorphous phase. The ice is then warmed to its "annealing" temperature, where the ice is then held at this temperature until it transitions to its lowest energy or crystalline phase; this phase transition is determined by various mechanisms depending on the investigator (*e.g.,* look for spectral changes that cease with time). However, this experimental approach is contradictory to the way in which ice clouds form in Titan's stratosphere. On Titan, atmospheric subsidence transports enriched trace organic vapors (dominantly nitriles and hydrocarbons) formed high above downwards to lower altitudes, leading to increased condensation in the cold, mid-to-low altitudes in Titan's winter polar stratosphere. Stratospheric condensation also occurs at mid and low latitudes, although the ice abundance is much lower than observed at the winter poles. Most of Titan's organic vapors will condense to form successive ice shells on Titan's photochemically-produced aerosol particles as the vapors cool while descending throughout Titan's stratosphere. Depending on vapor abundances, local atmospheric temperatures, and the saturation vapor pressures, these numerous chemical compounds will enter altitude regions in Titan's stratosphere where the vapors will simultaneously saturate, and co-condensation will commence. In the process of co-condensation, the ice particles will no longer be chemically isolated into successive shells of pure ices. Instead, a single uniform mixed ice layer will form, with continuously varying relative abundances as it subsides across the vertical range over which co-condensation is taking place. The concept of co-condensation as compared to that of layered ice particles is discussed further in §4. Lastly, in addition to vapor condensation formation processes, other ice formation processes, such as solid-state chemical processes, may also occur between adjacent pure/mixed ice shells to form new ice compounds in the solid state (see Anderson et al. 2016).

This paper describes the methodologies developed in the SPICE laboratory using the SPECTRAL chamber to better understand the chemical characteristics, optical and structural properties, and formation processes of Titan's stratospheric ice clouds as observed by CIRS. The SPECTRAL chamber is detailed in §2, while the synthesis of the pure vapors and purification procedures are described in §3. Thin ice film transmission measurements and optical constant calculations are discussed in §4, and concluding remarks are given in §5.

2. SPECTRAL ICE CHAMBER DESCRIPTION

A schematic of the SPECTRAL ice chamber is shown in Fig. 1. The ice chamber consists of an infrared spectrometer, cryostat, spherical sample chamber, turbo pump, UV lamp, quadrupole mass spectrometer, and two visible wavelength laser diodes.

Transmission spectra of vacuum deposited thin ice films ($<10\ \mu$m) are recorded with a Fourier Transform InfraRed (FTIR) spectrometer (Nicolet, model iS50R) spanning 50 to 11,700 cm^{-1} (200 to 0.85 μm). The FTIR spectrometer is fully-automated with multi-spectral range; the highest spectral resolution is $\Delta\nu = 0.09$ cm^{-1}. Typically, 256 scans are recorded at $\Delta\nu = 4$ cm^{-1}, then averaged, to produce a single spectrum. The spectrometer contains two internal sources – a Polaris^{TM} long-life IR source and a white light (Tungsten-Halogen) source, three beamsplitters, and three detectors for recording spectra across the far-, mid-, and near-IR spectral regions.

The far-IR beamsplitter (solid-state) spans 20 – 700 cm^{-1} (500 – 14.3 μm), the mid-IR beamsplitter (KBr) ranges from 350 to 7,400 cm^{-1} (28.6 to 1.35 μm), and the near-IR beamsplitter (CaF$_2$) covers the spectral range 1,200 – 14,500 cm^{-1} (8.3 – 0.69 μm). The far-IR detector (DTGS with polyethylene window) spans 50 – 700 cm^{-1} (200 – 14.3 μm), the LN$_2$-cooled mid-IR detector (MCT-A with CdTe window) ranges from 600 to 11,700 cm^{-1} (16.67 to 0.85 μm), and the additional mid-IR detector (DTGS with KBr window) spans 350 – 12,500 cm^{-1} (28.6 – 0.8 μm).

The FTIR spectrometer is controlled by the OMNIC^{TM} software (Thermo Scientific^{TM}). Depending on the selected detector, an Automated Beamsplitter Exchanger (ABX) loads the corresponding beamsplitter. This set-up allows for automatic transitioning across the far-, mid-, and near-IR spectral regions while keeping the purge intact. The purge is carried out by continuously flowing clean and dried compressed air into the spectrometer.

The FTIR spectrometer's main sample compartment permanently contains a spherical high-vacuum sample chamber (Kimball Physics; see Fig. 2). A circular (25.4 mm x 1 mm) Chemical Vapor Deposition (CVD) diamond substrate (Diamond Materials) resides at the center of the sample chamber, and is cooled by a closed-cycle cryostat (Advanced Research Systems, Inc.). The cryostat contains a cryocooler (Advanced Research Systems, Inc., model DE-202AI) connected to an air-cooled helium compressor (Advanced Research Systems, Inc., model ARS-125A). Connected to the cryocooler is a temperature controller (LakeShore, model 335) spanning temperatures 14 – 350 K ($\pm$ 13 mK at 1.4 K, $\pm$ 76 mK at 77 K, and $\pm$ 47 mK at 300 K), a 36-Ohm internal resistive Thermofoil heater wire that warms the diamond substrate, and two temperature sensors (silicon diodes; LakeShore, model 670B-SD) on the diamond substrate holder. Pressures as low as 6×10^{-8} Torr inside the high-vacuum sample chamber are maintained by a pumping station, which consists of a turbopump (Agilent Technologies, Inc., model TV 301 NAV) and a turbo rack controller (Agilent Technologies, Inc., model Turbo-V301-AG).

The spherical sample chamber has nine port windows (Fig. 2): two 2 3/4" Conflat Flange (CF) CVD diamond vacuum windows for transmission of the IR/white light source, two 1 1/3" CF quartz windows for the 635-nm and 532-nm laser diode incident beams (Thorlabs^{TM}, models CPS635F and CPS532, 5mW laser diodes), two 1 1/3" CF quartz windows for transmitting the reflected lasers to their corresponding Si photodiodes (Thorlabs^{TM}, model SM05PD1A), two 1 1/3" CF inlet lines for vapor deposition, and one 2 3/4" CF MgF$_2$ window used for irradiation experiments – it is connected to a vacuum ultraviolet (VUV) resonance mercury lamp filled with 3 Torr of argon (OPHTOS Instrument Company LLC), and emits two lines at 184.9 nm and 253.7 nm. A microwave generator (maximum power output of 120 W) is used to generate an argon discharge that excites the mercury, producing the two emission lines.

Thin ice films are grown by slowly depositing organic vapors via a variable leak valve onto the diamond substrate (detailed in §4.2). The diamond substrate is attached to the cryo-cooler's rotatable cold finger, located at the center of the spherical sample chamber (see Figs. 1 and 2). Both the deposition and flow rates are slightly variable, ranging from 0.1 to 0.5 μm/min and 0.02 to 0.2 μl/min, respectively, since both rates are functions of vapor composition and total gas pressure. The flow rate refers to an incoming gas as it enters the ice chamber to be condensed, and represents the volume of gas that passes through the gas inlet per unit time. On the other hand, the deposition rate refers to the production rate of an ice on the substrate, which describes the amount of ice that grows by vapor deposition per unit time.

Between the sub-mm and near-IR spectral regions, CVD diamond has excellent throughput with only one strong and broad absorption feature between $\sim$1900 and $\sim$2300 cm^{-1}($\sim$5.2 and $\sim$4.3 μm). Depending on the chemical compound, the loss of signal from the diamond absorption is partly correctable by optimizing the FTIR spectrometer's detector gain (the increase in the detector signal amplitude due to electronic amplification) and angular size (a variable diameter size that controls the input intensity of the IR/white light source). Using amorphous C$_2$N$_2$ (vapor deposited at 30 K) as an example, Fig. 3 illustrates the impact different combinations of detector gain, for a fixed aperture size, have on the strength of the diamond absorption feature. In practice, per chemical compound, several combinations of detector gain and aperture size are tested to obtain the best correction. The efficiency of this diamond-absorption recovery method is a function of the compound since ices have varying opacities – the more transparent the ice, the more difficult it is to mitigate the degree of diamond absorption since it is more affected by the diamond substrate.

As shown in Figs. 1 and 2, the two collimated laser diodes are mounted outside the vacuum chamber walls. The lasers are positioned at 55°and 65°, relative to the position of the growing thin ice film. The reflected laser signals are collected by two mounted photodiodes, which are connected to a compact data acquisition platform (National Instruments^{TM}, model NI cDAQ-91740) that measures their corresponding voltages. The voltage is monitored as a function of time for both lasers, and is carried out using a LabVIEW acquisition program. LabVIEW records the fringe patterns obtained from the two lasers simultaneously, which are then used as inputs into an IDL program to compute the refractive index at one of the laser wavelengths n_0 and the ice film thickness d. This is detailed in §4.

A quadrupole mass spectrometer (QMS; Pfeiffer^{TM}, model PrismaPlus) measures the ion masses from 1 to 200 amu of the vapors released as a result of sublimation at the end of the experiments. It is coupled to the same port as the VUV lamp via a 2 3/4" CF tee.

3. VAPOR SYNTHESIS AND PURIFICATION

The nitriles HCN, HC_3N, C_2N_2, and C_4N_2, all necessary for the Titan stratospheric ice experiments, are unavailable commercially so these compounds must be synthesized in the laboratory; Fig. 4 shows a spectrum of synthesized HCN. The syntheses are carried out using an 8-port glass vacuum manifold installed inside a fume hood and connected to a turbo-pumping station (Pfeiffer, model HiCube), which allows low pressures down to 5×10^{-6} mbar to be maintained. The volatile reaction products are examined during the synthesis with a Residual Gas Analyzer (RGA; Stanford Research Systems Inc.$^{®}$, Model RGA200), measuring ion masses from 1 to 200 amu.

The gaseous HCN monomer is synthesized by thermal reaction of equimolar potassium cyanide (KCN; Sigma Aldrich, 100%) and stearic acid (Sigma Aldrich, 97.2%) at ~100°C, following the procedure described in Gerakines et al. (2004). HC_3N is synthesized by reacting dry propiolamide (HC≡CCONH$_2$; Alfa Aesar, 98+%) with phosphorus pentoxide (P_2O_5; Sigma Aldrich, 98.6%) and dry sand (SiO$_2$; Sigma Aldrich, 100%) at ~225°C, adapted from the synthesis procedures of Moureu & Bongrand (1910), Miller & Lemmon (1967), and Graupner et al. (2006). C_4N_2 is synthesized by the reaction of dry 2-butynediamide (NH$_2$OC–C≡C–CONH$_2$; Acros Organics, 96.1%) with P_2O_5 and dry sand at ~230°C, following the methods of Moureu & Bongrand (1909), Moureu & Bongrand (1920), Miller & Hannan (1953), and Coll et al. (1999). C_2N_2 is synthesized by thermal decomposition of silver cyanide (AgCN; Alfa Aesar, 99%) following the procedures found in Hogness & Tśai (1932) and Brotherton & Lynn (1959). The dry salt must be heated at temperatures <300°C to prevent the formation of paracyanogen, the solid polymeric form of C_2N_2.

The syntheses of these nitriles generate byproducts from the reactions. Not only is it possible to introduce and/or form contaminants during the nitrile synthesis procedure, but the contaminants may also be present during handling and storage of the commercially purchased reactants. Moreover, in the presence of air contaminants such as moisture (H_2O) and carbon dioxide (CO_2), nitriles can rapidly react to form additional organics, and can also polymerize into CN polymers. Therefore, purifying the sample becomes critical, since the presence of a contaminant in the sample can alter the spectral features of the Titan ice analogs. To remove the contaminants, each experiment begins by depositing the vapor at 30 K, and then the resulting mid-IR recorded spectra are used to check the contamination level of the synthesized nitrile. This is an efficient analytical technique to detect major contaminants such as H_2O and CO_2, as well as minor organic byproduct contaminants that would otherwise be difficult to diagnosis in the far- or near-IR spectral regions. Once the contaminants are spectrally identified in the nitrile ice samples, their purification process is initiated by carrying out several freeze-thaw-pump cycles under vacuum, using an LN$_2$-ethanol slush bath (-116°C). With the adopted purification method, the contaminants H_2O and CO_2 have been successfully removed from the samples, as well as additional contaminants with abundances above the FTIR spectrometer detection limit. For example, during the purification process of C_2N_2, the ν_1 symmetric stretching mode of amorphous C_2N_2 at 2336 cm^{-1} was discovered, nominally masked by the asymmetric stretching mode of CO_2 at 2345 cm^{-1}. To our knowledge, only the liquid phase of C_2N_2 near 2336 cm^{-1} has been reported in the literature by Thomas & Orville-Thomas (1968) and Corain (1982). Although the 2336 cm^{-1} vibrational mode of C_2N_2 is expected to be IR-inactive, Thomas & Orville-Thomas (1968) report that in a condensed liquid phase, relaxation of the symmetry rules can occur. We only observe the 2336 cm^{-1} feature of C_2N_2 in the amorphous phase, and never in the crystalline phase. Figure 5 shows mid-IR spectra of the 2336 cm^{-1} feature of amorphous C_2N_2 ice (vapor deposited at 30 K), both with and without the CO_2-ice contamination in the sample.

Once the synthesis and purification procedures of the nitriles are completed, the pure CN gases are collected and condensed with LN$_2$ inside a valved glass tube. The resulting ice samples are then stored inside a -86°C ultra-low temperature freezer (Thermo-Scientific^{TM}, HFU 300T).

4. FAR- AND MID-IR SPECTROSCOPY

4.1. *Justification for co-condensed ice analogs*

Once a pure amorphous ice is sufficiently warmed (*i.e.,* annealed) or the vapor is deposited at a warm enough temperature, the molecules are able to mobilize into a crystalline structure, in which the electrical forces between the individual molecules are minimized. This gives rise to unique vibrational frequencies associated with a crystalline structure, which yields distinct spectral features. In a co-condensed ice, however, the ice is incapable of forming an ordered crystalline structure, and therefore the same degree of energy minimization cannot be achieved. This results in different vibrational frequencies from that of its pure ice counterparts, spectrally most evident in the low energy part of the far-IR, where lattice and librational modes dominate.

The SPECTRAL chamber is now operational, and in the beginning stages of detailed Titan ice analog (both pure and co-condensed) experimental studies. Preliminary results obtained from the SPECTRAL chamber are being used to identify the chemical compositions associated with some far-IR ice cloud spectral features observed in Titan's stratosphere by CIRS. One example is the ν_6 band of pure HC_3N at 506 cm^{-1} (19.8 μm), which was definitively identified in Titan's northern winter polar stratosphere (see Fig. 6; Anderson et al. 2010).

Another ice cloud example is the ν_8 band of C_4N_2 ice at 478 cm^{-1}, detected in Titan's early northern spring stratosphere (Fig. 7; Anderson et al. 2016). According to Anderson et al. (2016), the source of C_4N_2 ice may be the result of solid-state photochemistry, occurring inside extant particles of co-condensed HCN:HC_3N ice. Radiative transfer fits to the CIRS-observed Titan far-IR spectra for both pure C_4N_2 ice and a mixture containing 80% HCN ice and 20% C_4N_2 ice are shown in Fig. 7, clearly favoring the dilute mixture of HCN:C_4N_2 ice.

A third example has an ice emission feature that peaks at 160 cm^{-1} (62.5 μm; Figs. 6 and 8; see also Anderson & Samuelson 2011; Anderson et al. 2014). This stratospheric ice feature has a broad spectral dependence spanning the low energy part of the CIRS far-IR spectrum between ∼100 and 300 cm^{-1} (100 to 33.3 μm). This is an example in which the identification of an ice is more complex than for a pure ice since the ice emission feature arises from several chemical compounds (*i.e.,* a composite or mixed ice). The contribution from this composite ice emission feature to Titan's continuum is shown in Fig. 6 as the difference between the solid and dashed black curves (the stippled region), and would otherwise not be evident as an ice feature without a full radiative transfer analysis (Anderson & Samuelson 2011). As experimental work indicates, the 160 cm^{-1} stratospheric ice emission feature is a co-condensed ice resulting from the combination of the ν_7 band and lattice modes of HC_3N and the libration mode of HCN. As Fig. 8 demonstrates, a simple weighted sum of the pure HCN and pure HC_3N ice features considered separately will not fit this observed stratospheric ice emission feature. Instead, it is necessary to mix the two vapors together, deposit the vapor mixture (*i.e.,* reproducing co-condensation processes), and then derive the optical constants from thin film transmission spectroscopy of the mixed ice. The far-IR spectral dependence of the resulting mixed ice spectral feature is altered in spectral shape from that of the weighted sum of the individual ice features of HCN and HC_3N.

Both Figs. 8 and 9 demonstrate the importance of co-condensed ice experiments, as compared to that of co-addition ice experiments and layered ice experiments. Co-addition experiments involve depositing individual vapors in separate experiments and then co-adding the resulting absorbances (and/or imaginary part of the refractive indices) of the pure ices – this mimics a layered ice; examples are shown with HCN ice and C_2N_2 ice in Fig. 9 and with HCN ice and HC_3N ice in Fig. 8. Layered ice experiments involve depositing individual vapors one at a time during a given experiment *i.e.,* one compound is deposited and after a certain thickness is achieved, another compound with a different chemical composition is deposited on top of the first. Co-condensed ice experiments involve mixing two or more vapors first and then depositing the vapor mixture. However, while co-added and layered ices mimic each other, neither adequately reproduces the optical and structural properties and the chemical composition of the resulting co-condensed ice, especially in the low energy part of the far-IR (*i.e.,* <400 cm^{-1}); this effect is illustrated with HCN ice and C_2N_2 ice in Fig. 9. Figure 9 shows the difference between an 8.33-μm thick film of a composite ice containing 50% HCN and 50% C_2N_2, compared to that of a 4.31-μm thick film of HCN ice layered on a 4.34-μm thick film of C_2N_2, all vapors deposited at 110 K. As indicated in the figure, it becomes easier to distinguish between layered and co-condensed ices with decreasing energy (going to lower wavenumbers). Specifically, for the HCN:C_2N_2 ice mixture, the presence of C_2N_2 appears to have a catastrophic effect on HCN – it significantly damps out the absorption strength of all the HCN vibrational modes shown, a result that is never observed in the layered ices. In addition to the decrease in the HCN absorption strengths, the HCN vibrational bands shown also suffer a peak wavenumber shift to higher energies, as compared to the layered and co-added ices. On the other hand, however, C_2N_2 appears to be relatively

unaffected by the presence of HCN in the mixture – C_2N_2 appears rather stable regarding its absorption strength, spectral shape, and peak wavenumber position.

4.2. *Vapor Deposition Methodology*

As discussed earlier, reproducing ice cloud formation in Titan's stratosphere requires the organic vapor to be deposited at warmer temperatures (*e.g.,* 110 K). In practice, there are inherent differences between depositing the vapor directly at warmer temperatures compared with depositing the vapor at colder temperatures (*e.g.,* 30 K), and then warming to convert the ice to the crystalline phase. The latter approach forces the ice into its amorphous phase before being warmed to its annealing temperature. The ice is then held at its annealing temperature until the structure transitions to its crystalline phase. However, during annealing experiments, a portion of the ice's amorphous structure is irreversibly retained even after the crystalline phase has been achieved. This is most noticeable in the low energy lattice modes, and is discussed in greater detail for propionitrile (C_2H_5CN) in Nna-Mvondo et al. (2018).

Although depositing the vapor directly into the amorphous phase has been the standard practice for decades regarding Titan stratospheric ice studies (Khanna et al. 1988; Masterson & Khanna 1990; Dello Russo & Khanna 1996; Khanna 2005; Moore et al. 2010), this approach limits the understanding and reproduction of Titan's stratospheric ices, especially for the Cassini CIRS-discovered composite ices discussed earlier. Even so, there are four reasons to deposit the vapor at cold temperatures. Firstly, there is the need to compare with previous published measurements. Secondly, in order to test for contaminants (*e.g.,* CO_2; see §3), the vapor is deposited at a cold temperature in the mid-IR and, if it is impure, the purification procedures are initiated (§3). Thirdly, with co-condensed or mixed ices, the distinction between the amorphous and crystalline phase is often unclear, and the saturation vapor pressures for the gas mixtures are not necessarily equivalent to those of their pure counterparts (F. Raulin, personal communication). Numerous temperatures must be studied for the compounds of interest in both their pure and mixed states in order to fully understand the chemical and structural changes occurring within an ice as it forms during co-condensation processes. Lastly, studying hydrocarbon and nitrile ices in their amorphous phase has relevance for other planetary objects than that of Titan (*e.g.,* the Pluto system).

The organic vapors are typically deposited at 30 K, 60 K, 90 K, and 110 K (or 120 K), although intermediate and warmer/cooler temperatures are utilized as needed, depending on the compound being studied. In order to compare the experimental data with previous published work on pure ices, the vapors are also deposited at 30 K or 60 K and then the ice is warmed until the annealing temperature is met. The ice is held at this temperature until the crystalline phase has been achieved. For both annealing and warm-depositing experiments, the crystalline temperature is assessed based on two criteria: 1) there are no observed changes in the strength and/or spectral dependence of the absorption bands after a 24-hour period, and 2) there is no noticeable sublimation of the ice film at the held temperature during the 24-hour time period. See Nna-Mvondo et al. (2018) for more details.

4.3. *Determination of Optical Constants*

As the ice film grows with deposition time, the interference fringe patterns are measured from the reflected ice layers at 532 nm and 635 nm (illustrated in Fig. 10). From these resulting interference fringe patterns, the ice thickness d and the refractive index n_0 can be determined, since n_0 typically varies by less than 1% between 532 nm and 635 nm. The ice thickness d is related to the number of interference peaks seen in the fringe time-dependent voltage patterns via the Bragg equation (see Tempelmeyer & Mills Jr. 1968; Domingo et al. 2007, and references therein):

$$d = \frac{m\lambda}{2\sqrt{n_0^2 - \sin^2\theta}}, \tag{1}$$

where λ is the wavelength of the laser diodes at either 532 nm or 635 nm, m is the number of phases present in each of the two interference fringe patterns, n_0 is the real part of the refractive index of the ice at λ, and θ is the incident angle of each of the two incoming lasers normal to the substrate surface. Voltage peaks in the interference fringe patterns occur at integer values of m; voltage minima are located at half-integer values of m. A custom IDL program was developed to automatically locate the fringe extrema for each wavelength in order to calculate m as a function of time. The m-time series for the 532-nm laser is then cubic spline interpolated onto the times where the 635-nm interference fringe pattern peaks. This provides simultaneous measurements of m at both wavelengths that are used with Eq. 1 to solve for n_0. Following this, the median of these n_0 values is calculated and the 1σ uncertainty

is estimated using the Median Absolute Deviation (MAD). For the 110 K-deposited HCN ice fringe patterns shown in Fig. 10, an n_0 of 1.35 ± 0.014 was determined. Moore et al. (2010) reported HCN n_0 values of 1.3 at 30 K and 1.39 at 120 K, using a 670 nm wavelength laser. On the other hand, Masterson & Khanna (1990) determined an n_0 value of 1.36 (deposited at 60 K then annealed at 80 K, and then cooled to 60 K), although the laser wavelength is not discussed. Dello Russo & Khanna (1996) deposited HCN at a temperature somewhere between 50 and 100 K, annealed at 120 K, then cooled to 95 K. The n_0 value, however, is not reported. The variations amongst the reported n_0 values are most likely due to changing experimental conditions *i.e.,* laser incident angles, deposition temperatures, deposition/annealing methodology, vapor flow rates, ice phase, etc.

Once n_0 is known, it is then input into Eq. 1 to compute the thin ice film thickness d at the last maxima in the interference fringe pattern. The 1σ uncertainty in d is then calculated through standard error propagation using the MAD-determined uncertainty in n_0. Using the 635-nm interference fringe pattern shown in Fig. 10, the calculated thickness for the HCN ice sample is 1.90 ± 0.04 μm.

In order to compute the optical constants, in addition to input parameters d and n_0, the third input parameter is the channel fringe-corrected experimental absorbance spectrum, A_ν. To remove the channel fringes, an IDL program was developed that takes the inverse Fast Fourier Transform (FFT) of the experimental spectrum to generate a time-domain interferogram. In interferogram space, it is easy to locate the index value of the dominant optical path difference of the channel fringes, with signatures that resemble spikes. To suppress the spikes, a bandpass filter is effectively applied by multiplying the interferogram by a window function, and then fourier transforming this product back to spectral space. As discussed in Hirschfeld & Mantz (1976), reducing a few points out of thousands results in a less than 0.1% change in the line shape and intensity. Suppressing the spikes, however, creates slight spectral distortions near the spectral peaks, which results from phase errors introduced by the discontinuities in the spike-suppressed interferogram (see Hirschfeld & Mantz 1976, for further explanation). To recover the signal loss from the distortions, a cubic spline interpolation is applied across the continuum of the affected spectral region, and then subtracted off from the data. Resulting spectra from the data processing method are illustrated with HCN ice in Fig. 4.

To compute the real and imaginary parts of the ice refractive index, a custom IDL program was developed, which uses Lambert-Beer's law and applies an iterative Kramers-Kronig analysis of the experimentally-measured IR absorbance spectrum. The imaginary part of the refractive index, $k(\nu)$, is determined from the equation

$$k(\nu) = \frac{\alpha(\nu)}{4\pi\nu}, \tag{2}$$

where $\alpha(\nu)$, the Lambert absorption coefficient, is initially estimated from the quotient $[A_\nu/d]$; d is the thin ice film thickness, A_ν is the channel fringe-corrected experimental absorbance spectrum, and ν is the wavenumber in cm^{-1}. The Kramers-Kronig relationship is then used to calculate the initial estimate of the real part of the refractive index $n(\nu)$ from the equation

$$n(\nu) = n_0 + \frac{2}{\pi} \int_{\nu_1}^{\nu_2} \frac{\nu' k(\nu')}{\nu'^2 - \nu^2} d\nu', \tag{3}$$

where n_0 is the real part of the refractive index at one optical wavelength determined from Eq. 1 and ν_1 and ν_2 are the minimum and maximum of the wavenumber range over which the integration occurs; the calculations also avoid the divergent point $\nu'=\nu$. The iteration continues by using the initial estimates of $k(\nu)$ and $n(\nu)$ as input into the fully expanded Lambert absorption coefficient equation, $\alpha(\nu)$, defined by Rocha & Pilling (2014) and references therein:

$$\alpha(\nu) = \frac{1}{d} \left(A_\nu + ln \left| \frac{t_{01} t_{12}/t_{02}}{1 + r_{01} r_{12}} \right|^2 \right), \tag{4}$$

where the Fresnel coefficients t and r represent the complex transmission and reflection, and the subscripts 0, 1, and 2 refer to the vacuum, ice sample, or diamond substrate, respectively. For normal incidence, the Fresnel coefficients are typically defined using the pq notation: $t_{pq} = 2\,m_p/(m_p + m_q)$ and $r_{pq} = (m_p - m_q)(m_p + m_q)$, where the p and q terms represent the vacuum, ice sample, or diamond substrate (0, 1, or 2) and the pq notation designates the interfaces

between these regions. The m term represents the complex refractive indices, defined by $m = n + ik$. For more details see Chopra (1969); Masterson & Khanna (1990); Rocha & Pilling (2014).

Next, $\alpha(\nu)$ is inserted into Eq. 2, and the new $k(\nu)$ values are computed and then inserted into Eq. 3 to determine the next values of $n(\nu)$. The iteration continues until $n(\nu)$ and $k(\nu)$ converge to their final values, which occurs in practice in just a few iterations.

To test the accuracy of this iterative procedure, the final $n(\nu)$ and $k(\nu)$ values are used to compute the theoretical transmission spectrum for the compound(s) being studied, using Eq. 5 in Rocha & Pilling (2014). Lastly, the errors between the channel fringe-corrected experimental and theoretical absorbance spectra are evaluated using the Mean Absolute Percentage Error (MAPE), and are typically less than 0.001%.

All of the absorbance spectra and corresponding optical constant calculations will be added to the SPICE Lab website as they become available: https://science.gsfc.nasa.gov/spicelab/.

4.4. *Connection between refractive indices and the CIRS-observed ice abundances*

CIRS spectra are fit by solving the radiative transfer equation, which gives the ice volume extinction coefficient $N\chi_E$ (see Anderson et al. 2010; Anderson & Samuelson 2011; Anderson et al. 2014, 2016, for further explanation). $N\chi_E$ is the product of the number density of the ice particles N and the optical extinction cross section per ice particle χ_E. In general, in order to obtain N and χ_E separately, additional information is needed. This consists of the refractive indices n and k and the ice particle radius a. In the thermal IR, the size of the particle is typically inferred from the spectral shape of the observed ice emission feature using Mie theory. Once n, k, and a are known, χ_E can then be computed, *e.g.,* with Mie theory. Once χ_E is known, N can then be calculated, from which the number of ice molecules contained in a volume element q (or ice mole fraction) can then be determined.

We illustrate with one example. Figure 11 shows the relationship between n, k, and χ_E for both pure HCN ice and a composite ice containing 39% HCN and 61% C_6H_6, all vapors deposited at 110 K. In the figure, the normalized extinction cross-section χ_E is computed using the small particle limit from Eq. 8.4.2 in Hanel et al. (2003):

$$N\chi_E = 48\pi^2 a^3 \nu N \left(\frac{nk}{(n^2 - k^2 + 2)^2 + 4n^2k^2} \right), \tag{5}$$

where N is the ice particle number density, χ_E is the optical extinction cross section per ice particle, a is the effective particle radius, ν is the wavenumber, and n and k are the refractive indices. As shown in Fig. 11, the spectral dependence of pure HCN ice looks very different than that of the HCN:C_6H_6 co-condensed ice. These differences are noticeable in n, k, and χ_E. The extinction cross sections for both the libration mode and ν_2 bending mode of pure HCN ice shifts to higher wavenumbers in the composite ice when HCN ice is diluted in the HCN:C_6H_6 mixture. This is partly due to n becoming more symmetrical about the central emission feature near 168 cm^{-1} and 827 cm^{-1}, and also to k shifting to higher wavenumbers in the composite ice.

5. CONCLUDING REMARKS

The SPECTRAL chamber was designed and built with the main purpose of determining the chemical compositions, structural and optical properties, and formation processes of Titan's CIRS-observed stratospheric ice clouds. The three examples described in §4, which compare Titan's CIRS-observed stratospheric ice clouds to laboratory ice spectra, demonstrate the critical need for performing laboratory thin film transmission spectroscopy of both pure and mixed organic ices. Moreover, additional stratospheric ice cloud features observed by CIRS, which are more complex and not discussed here, have proven even more difficult to identify. One example is the unidentified stratospheric emission feature at 221 cm^{-1} (see Fig. 6), which we call the Haystack; it is presumed to be a stratospheric ice cloud (see Jennings et al. 2012a,b; Anderson et al. 2014; Jennings et al. 2015). Another ice feature is associated with our more recent CIRS discovery – Titan's High-Altitude South Polar (HASP) cloud (Anderson et al. 2017), which is spectrally centered at roughly 210 cm^{-1}, and found at relatively high altitudes in Titan's south polar stratosphere during late southern fall. Analyses of both stratospheric ice features using the SPECTRAL chamber are currently underway.

REFERENCES

Anderson, C., Nna-Mvondo, D., Samuelson, R. E., et al. 2017, in AAS/Division for Planetary Sciences Meeting Abstracts, Vol. 49, AAS/Division for Planetary Sciences Meeting Abstracts #49, 304.10

Anderson, C. M., & Samuelson, R. E. 2011, Icarus, 212, 762

Anderson, C. M., Samuelson, R. E., Achterberg, R. K., Barnes, J. W., & Flasar, F. M. 2014, Icarus, 243, 129

Anderson, C. M., Samuelson, R. E., Bjoraker, G. L., & Achterberg, R. K. 2010, Icarus, 207, 914

Anderson, C. M., Samuelson, R. E., Yung, Y. L., & McLain, J. L. 2016, Geophys. Res. Lett., 43, 3088

Brotherton, T. K., & Lynn, J. W. 1959, Chem. Rev., 59, 841

Chopra, K. L. 1969, Thin Film Phenomena (McGraw-Hill, New York)

Coll, P., Guillemin, J.-C., Gazeau, M.-C., & Raulin, F. 1999, Plan. & Space Sci., 47, 1433

Corain, B. 1982, Coordination Chemistry Reviews, 47, 165

Coustenis, A., Schmitt, B., Khanna, R. K., & Trotta, F. 1999, Plan. & Space Sci., 47, 1305

de Kok, R., Irwin, P. G. J., Teanby, N. A., et al. 2007, Icarus, 191, 223

Dello Russo, N., & Khanna, R. K. 1996, Icarus, 123, 366

Domingo, M., Millán, C., A., S. M., & Canto, J. 2007, Optical Measurement Systems for Industrial Inspection, 66164A, 1

Frere, C., Raulin, F., Israel, G., & Cabane, M. 1990, Adv. Space Res., 10, 159

Gerakines, P. A., Moore, M. H., & Hudson, R. L. 2004, Icarus, 170, 202

Graupner, M. K., Field, T., Youngs, T., & Marr, P. 2006, New J. Phys, 8, 117

Hanel, R., Conrath, B., Flasar, F. M., et al. 1981, Science, 212, 192

Hanel, R. A., Conrath, B. J., Jennings, D. E., & Samuelson, R. E. 2003, in Exploration of the Solar System by Infrared Remote Sensing (Cambridge, New York, Port Chester, Melbourne, Sydney: Cambridge University Press), 352–404

Hirschfeld, T., & Mantz, A. W. 1976, Applied Spectroscopy, 50, 5532

Hogness, R. T., & Tśai, L. S. 1932, J . Amer. Chem. Soc, 54, 123

Jennings, D. E., Anderson, C. M., Samuelson, R. E., et al. 2012a, Astrophys. J. letters, 754, L3

—. 2012b, Astrophys. J. letters, 761, L15

Jennings, D. E., Achterberg, R. K., Cottini, V., et al. 2015, Astrophys. J. letters, 804, L34

Khanna, R. K. 2005, Icarus, 178, 165

Khanna, R. K., Ospina, M. J., & Zhao, G. 1988, Icarus, 73, 527

Maguire, W. C., Hanel, R. A., Jennings, D. E., Kunde, V. G., & Samuelson, R. E. 1981, Nature, 292, 683

Masterson, C. M., & Khanna, R. K. 1990, Icarus, 83, 83

Miller, F. A., & Hannan, R. B. 1953, J. Chem. Phys., 21, 110

Miller, F. A., & Lemmon, D. H. 1967, Spectrochim. Acta, 23A, 1415

Moore, M. H., Ferrante, R. F., Moore, W. J., & Hudson, R. 2010, Astrophys. J. Supp., 191, 96

Moureu, C., & Bongrand, J. C. 1909, Bulletin de la Société chimique de France. Mémoires, 846

—. 1910, Académie Des Sciences, 946

—. 1920, Ann. Chem., 14, 47

Nna-Mvondo, D., Anderson, C. A., & Samuelson, R. E. 2018, Icarus, in preparation

Raulin, F., & Owen, T. 2002, Space Sci. Rev., 104, 377

Rocha, W., & Pilling, S. 2014, Spectrochimica Acta Part A: Molecular and Biomolecular Spectroscopy, 123, 436

Sagan, C., & Thompson, W. R. 1984, Icarus, 59, 133

Samuelson, R. E., Mayo, L. A., Knuckles, M. A., & Khanna, R. J. 1997, Plan. & Space Sci., 45, 941

Samuelson, R. E., Smith, M. D., Achterberg, R. K., & Pearl, J. C. 2007, Icarus, 189, 63

Tempelmeyer, K. E., & Mills Jr., D. W. 1968, Journal of Applied Physics, 39, 2968

Thomas, B. H., & Orville-Thomas, W. J. 1968, Journal of Molecular Structure, 3, 191

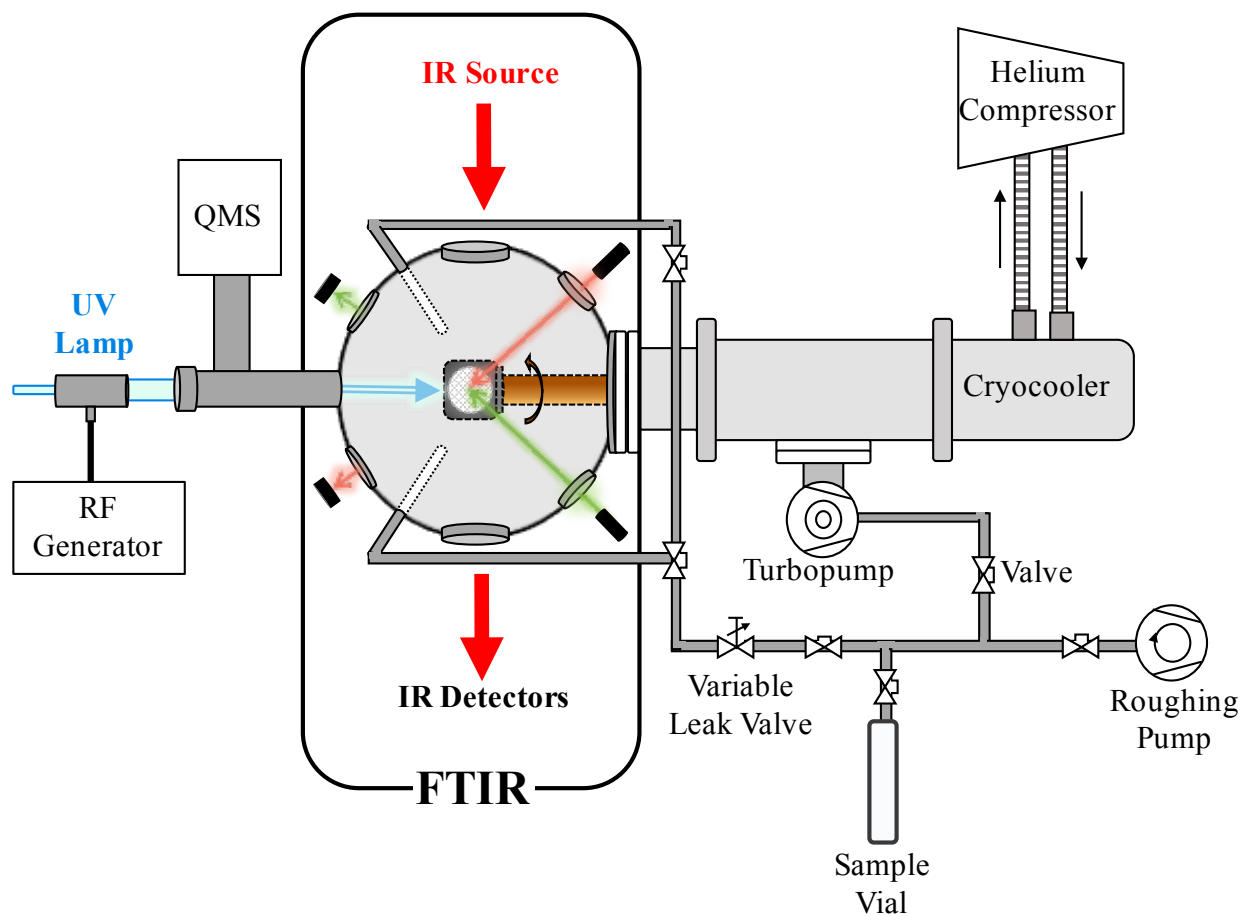Vinatier, S., Schmitt, B., Bézard, B., et al. 2018, Icarus, 310, 89

Figure 1. Schematic of the SPECTRAL ice chamber experimental setup at NASA Goddard Space Flight Center (GSFC). Both pure and mixed vapors are deposited between 30 K and 150 K via a variable leak valve onto a cooled Chemical Vapor Deposition (CVD) diamond substrate (small circular stippled region; see Fig. 2), where condensation occurs directly into the solid phase. Transmission spectroscopy across the far- to near-IR ($50 - 11{,}700$ cm^{-1}; $200 - 0.85$ μm) is then used to detect absorption bands arising from the ices, from which optical constants can then be determined.
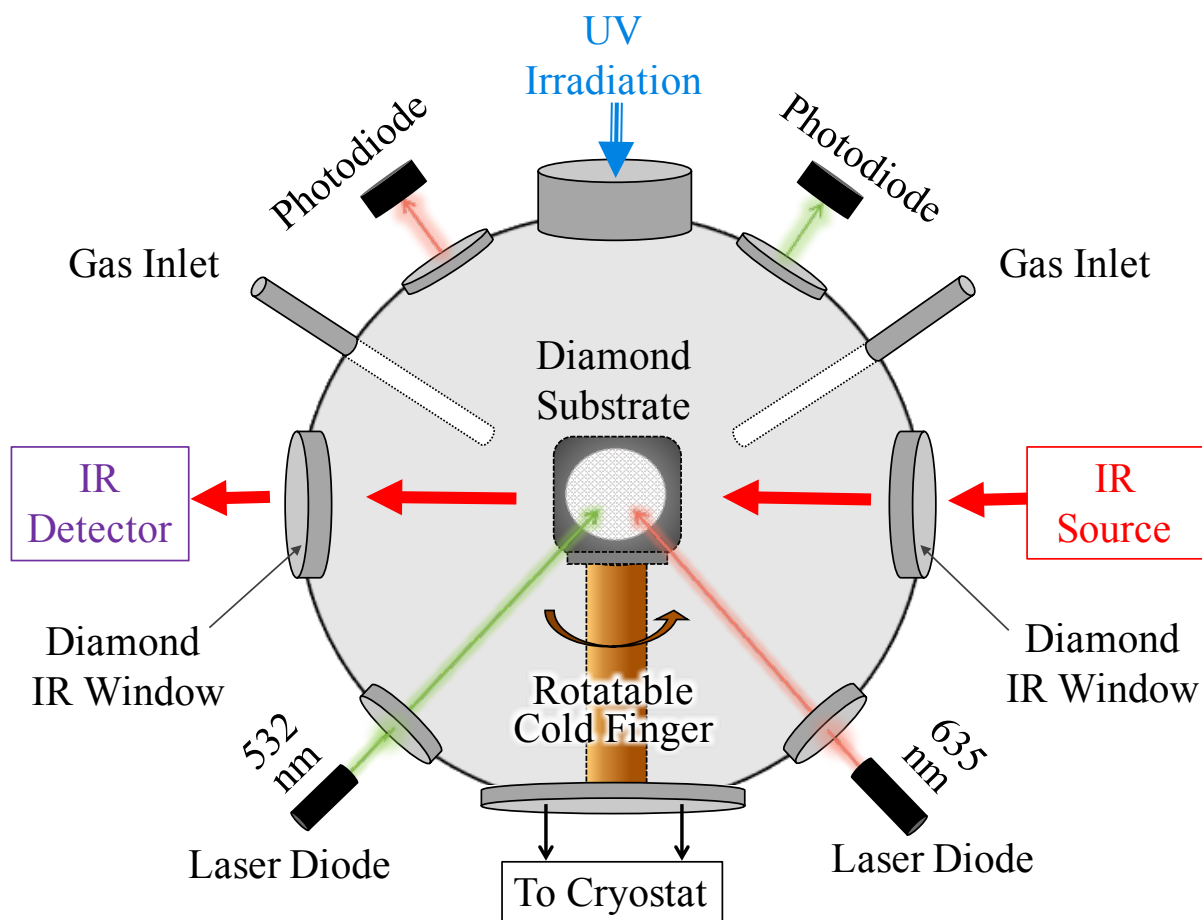
Figure 2. Schematic of the spherical high-vacuum sample chamber that permanently resides in the FTIR spectrometer's main sample compartment. The spherical chamber has nine port windows: two 2 3/4" Conflat Flange (CF) IR/white light source *in* and *out* CVD diamond vacuum windows, two 1 1/3" CF laser diode windows, positioned at incident angles of 55° and 65° relative to the 25 mm × 1 mm CVD diamond substrate, two 1 1/3" CF photodiode windows, positioned at 55° and 65°, two 1 1/3" windows for vapor deposition, both positioned at 45°, and one 2 3/4" CF irradiation window.
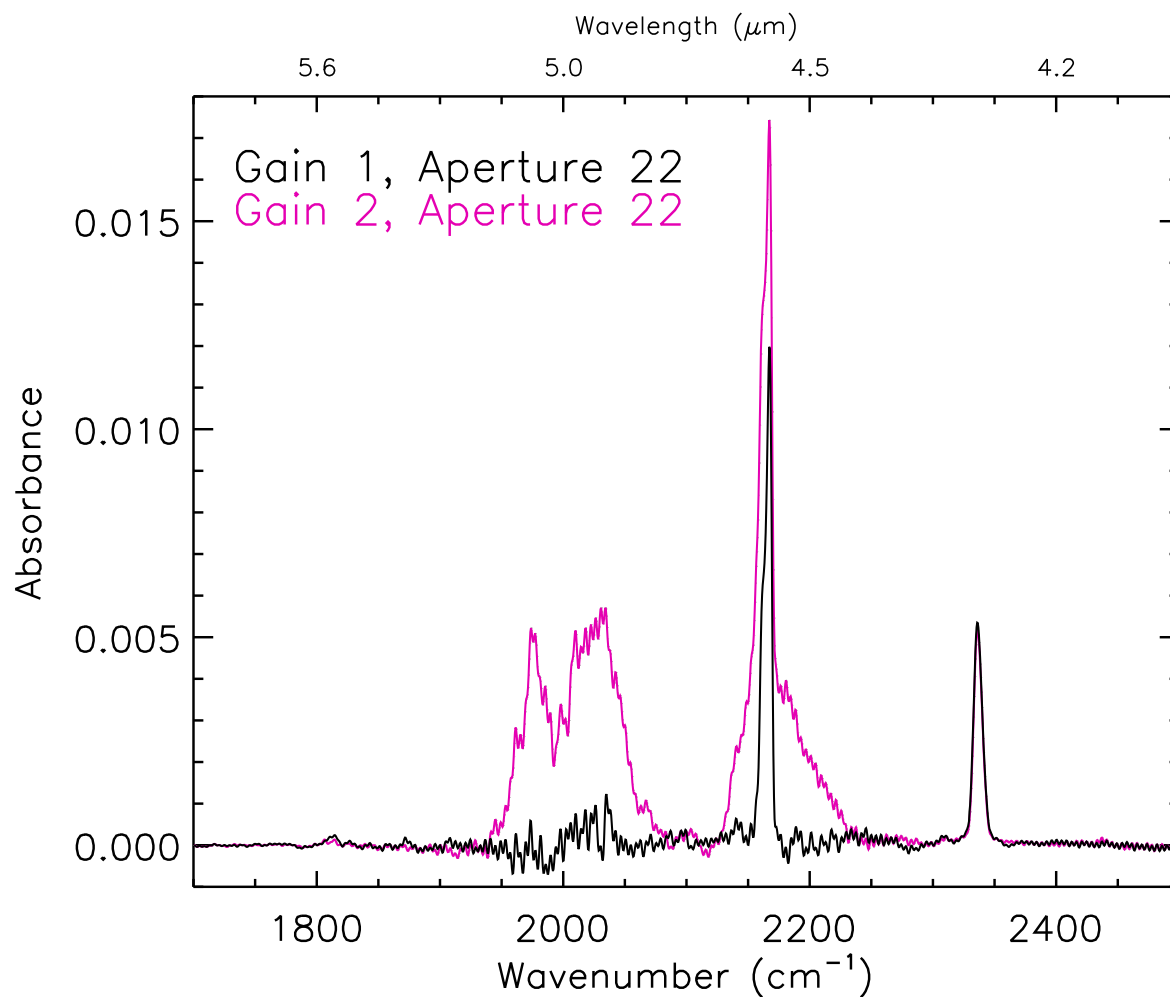
Figure 3. Absorbance spectra of a 4.19-μm thick film of amorphous C_2N_2 (vapor was deposited at 30 K). The two curves depict two different combinations of detector gain for one fixed aperture size. The pink curve shows the combination of gain 2 and aperture size 22, while the black curve depicts the combination of gain 1 and the same aperture size (22). The latter combination is optimal for C_2N_2 ice. For each chemical compound, several combinations of detector gain and aperture size are assessed in order to optimize the minimization of the CVD diamond absorption band strength between $\sim$1900 and $\sim$2300 cm^{-1} ($\sim$5.2 and $\sim$4.3 μm).
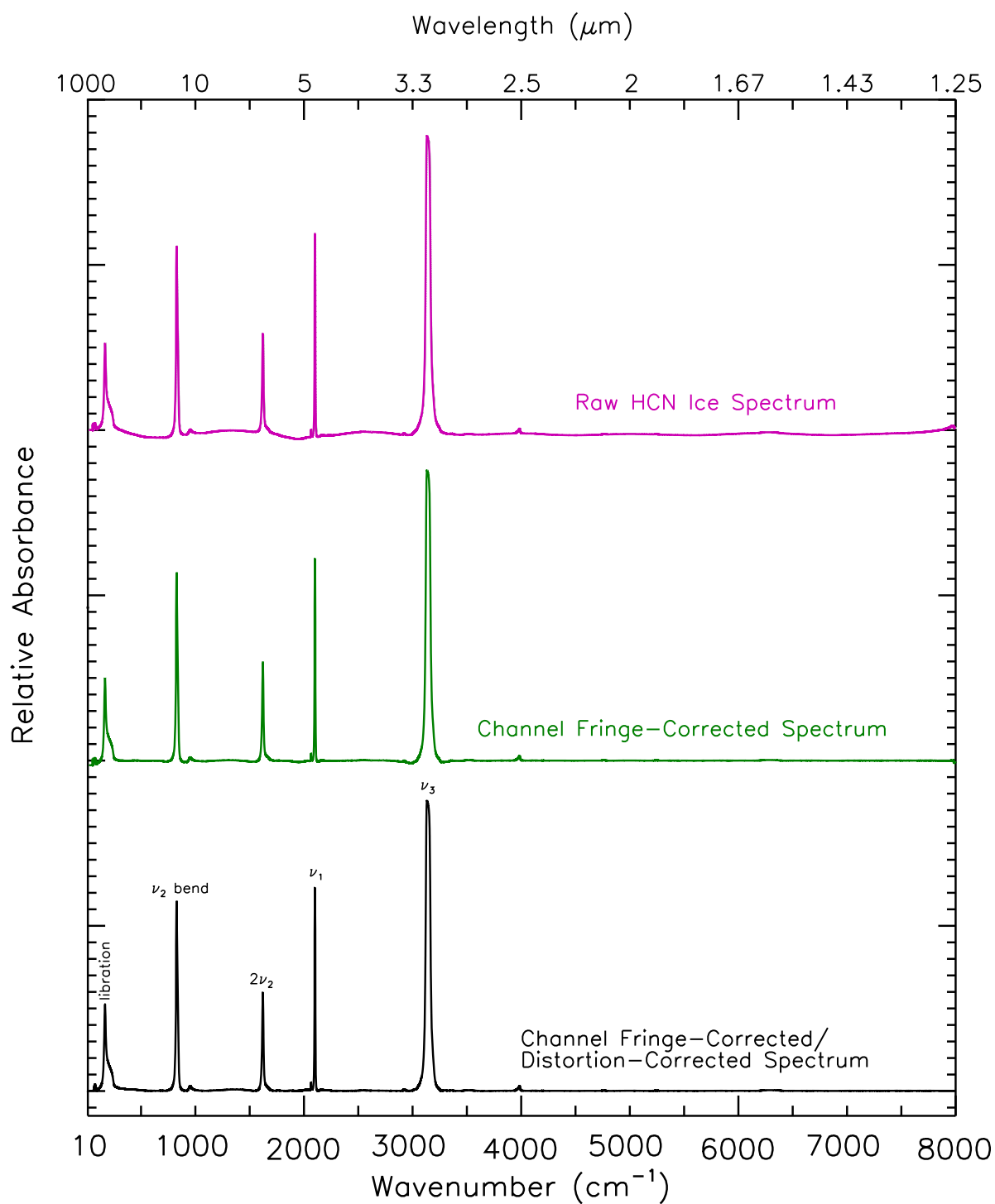
Figure 4. Absorbance spectra of a 4.29-μm thick film of HCN ice (vapor deposited at 110 K). The top spectrum (pink curve) represents the raw experimental HCN ice spectrum, showing the channel fringes. The middle spectrum (green curve) illustrates the first stage of the data processing, which removes the channel fringes. The bottom spectrum (black curve) depicts the final data processing stage, free of channel fringes and also spectral distortions, the latter of which is introduced during the channel fringe removal procedure (see §4 for details on the data processing method).
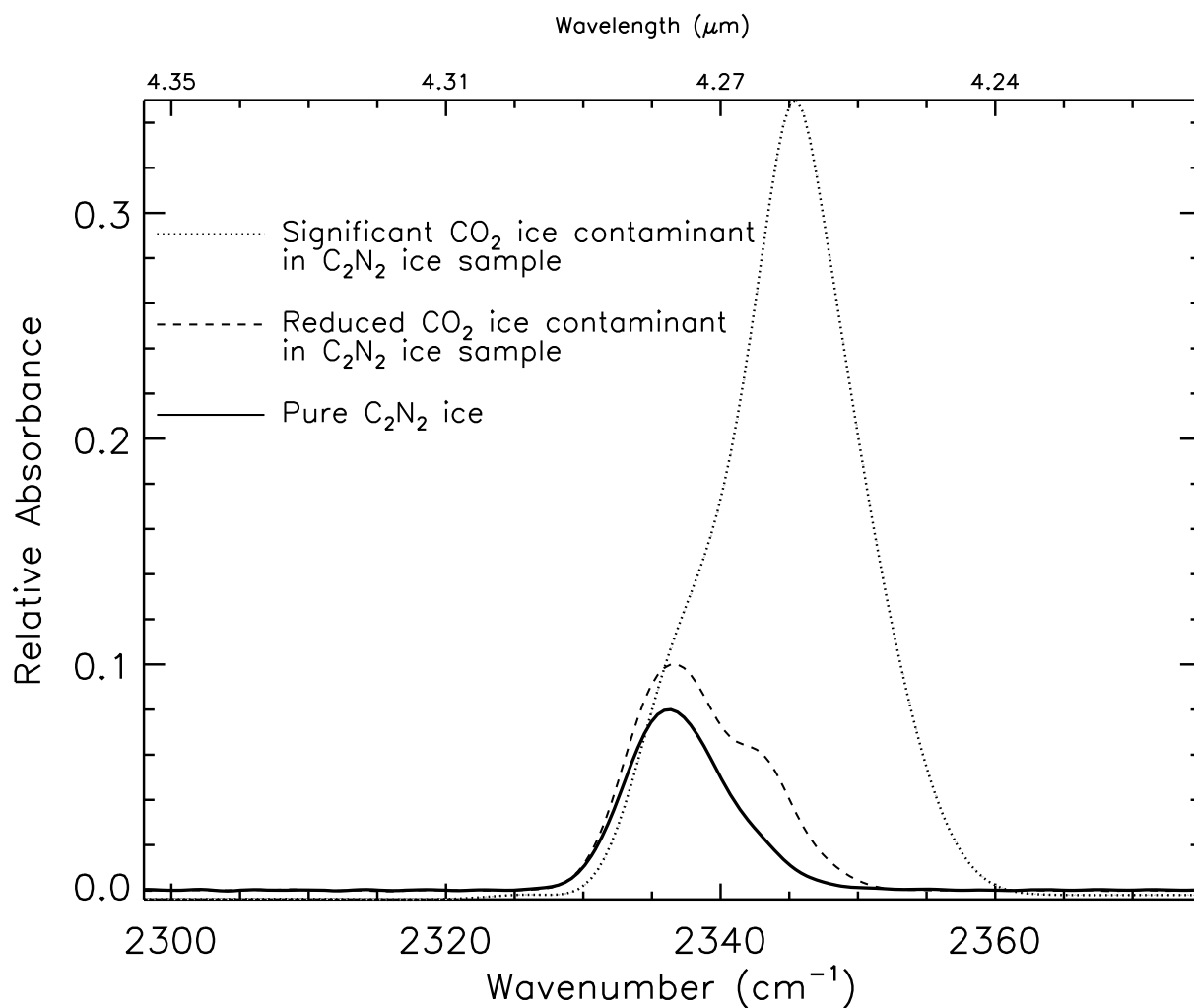
Figure 5. Mid-IR spectra of a 4.16-μm thick film of amorphous C_2N_2 ice (vapor deposited at 30 K). The three different curves illustrate the degree of CO_2 ice (asymmetric stretching mode at $\sim$2345 cm^{-1}) contamination in the C_2N_2 sample, following C_2N_2 synthesis. The black dotted curve shows the C_2N_2 ice sample dominated by CO_2 ice contamination ($\sim$16:1), masking the amorphous C_2N_2 feature at 2336 cm^{-1}. The black dashed curve shows the C_2N_2 ice sample with a reduced amount of contamination from CO_2 ice ($\sim$3:1) after numerous freeze-thaw-pump cycles in an LN$_2$-Ethanol cold bath (116°C). The solid black curve reveals the ν_1 symmetric stretch of C_2N_2 ice at 2336 cm^{-1}(any CO_2 contamination is now below the spectrometer's detection level), following additional freeze-thaw-pump cycles.
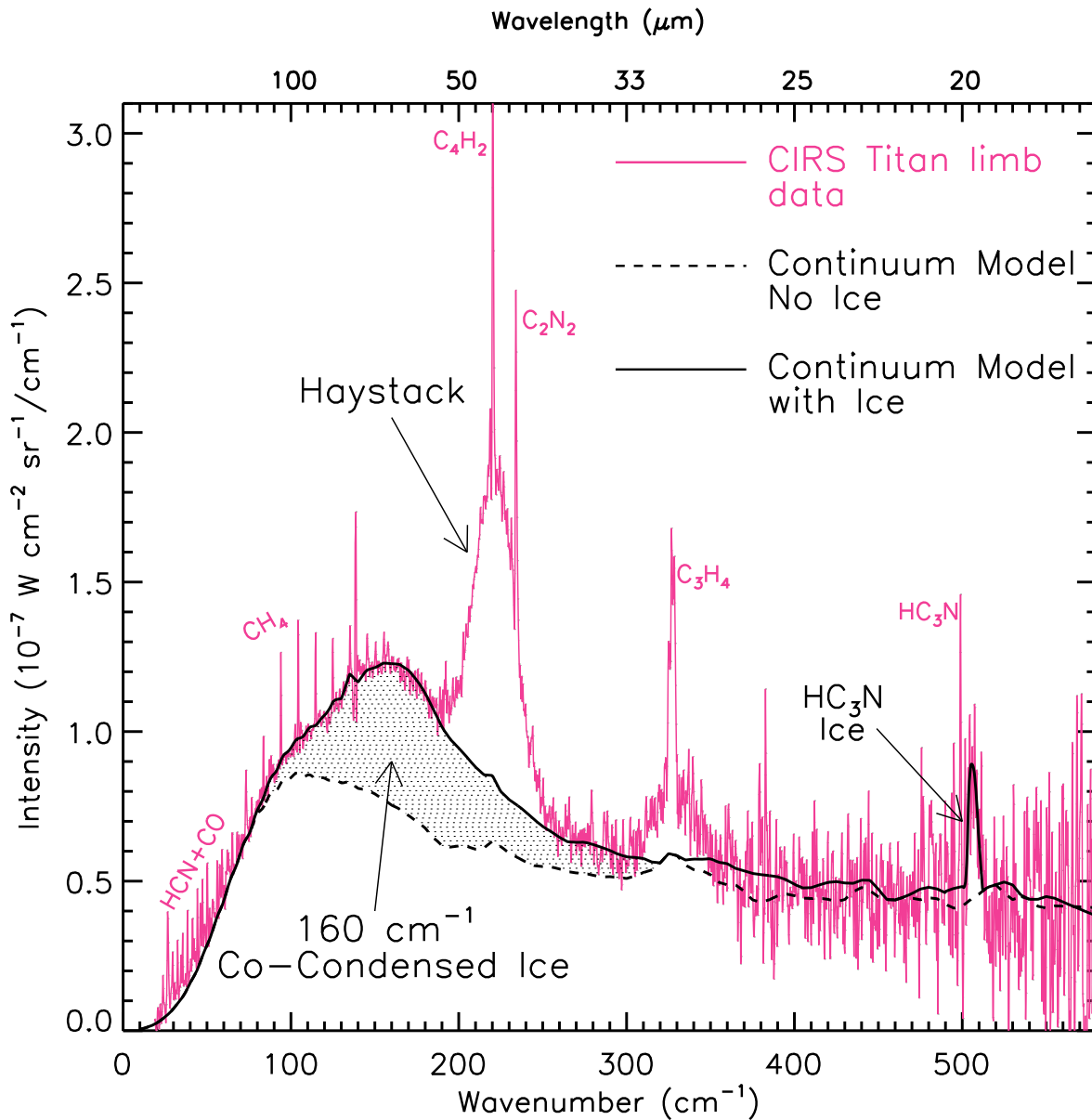
Figure 6. Modified from Anderson et al. (2014). Cassini CIRS far-IR limb integration spectrum (solid pink curve; $\Delta\nu$= 0.48 cm^{-1}) of Titan recorded at 62°N latitude and a 125-km tangent height during mid-to-late northern winter (July 2006). The assortment of organic vapors observable by CIRS are labeled, as is an unidentified broad ice emission feature centered at ~221 cm^{-1} – the Haystack – and the ν_6 band of HC$_3$N ice at 506 cm^{-1}. Noticeable as well in the limb spectrum is the broad ice emission feature that peaks at 160 cm^{-1}, whose contribution to the continuum is indicated by the stippled region. Without the 160 cm^{-1} co-condensed ice feature, the continuum would reduce to the dashed curve level, demonstrating the significance of the stratospheric ice cloud. No attempt is made to include either the various observed vapor emission features or the Haystack in the radiative transfer fit (*i.e.,* only the continuum opacity sources are included in the fit).
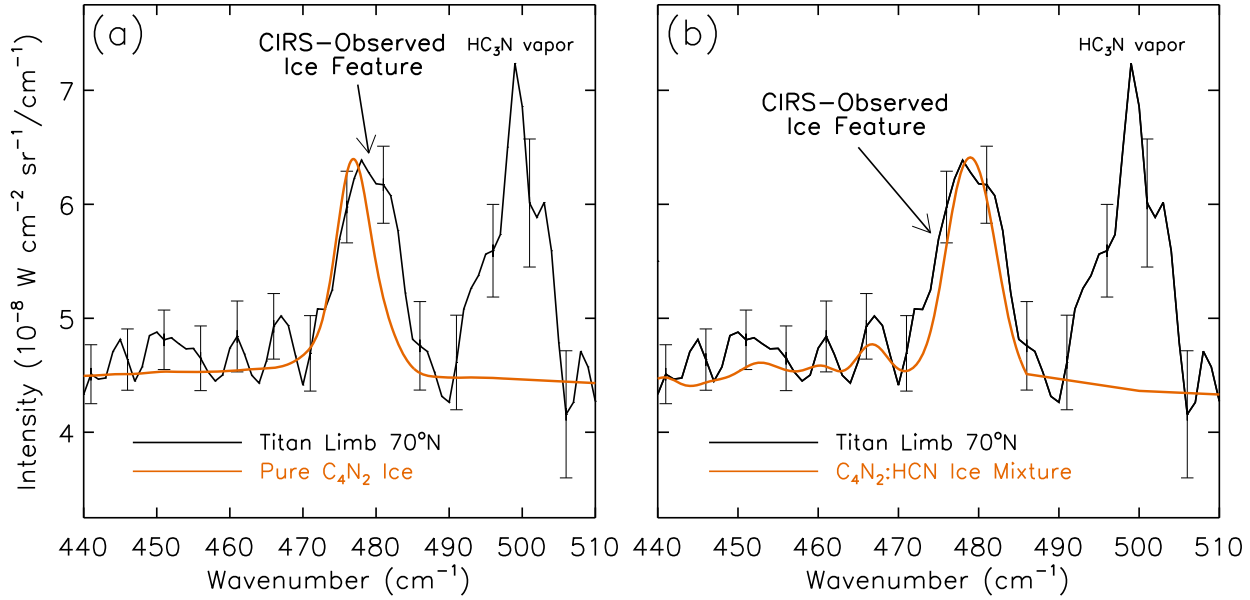
Figure 7. Modified from Anderson et al. (2016). Cassini CIRS far-IR limb integration spectrum (solid black curve; $\Delta\nu = 2.56$ cm^{-1}) of Titan recorded at 70°N latitude and a ~150-km tangent height during early northern spring (April 2010). Orange solid curves depict radiative transfer calculations using SPICE lab-determined n and k values for (a) pure C_4N_2 ice and (b) a co-condensed ice mixture containing 20% C_4N_2 and 80% HCN; both experiments deposited the vapors at 110 K. As C_4N_2 becomes more diluted in HCN within the ice mixture, the resulting composite ice analog emission feature shifts to higher wavenumbers, yielding better fits to the CIRS data.
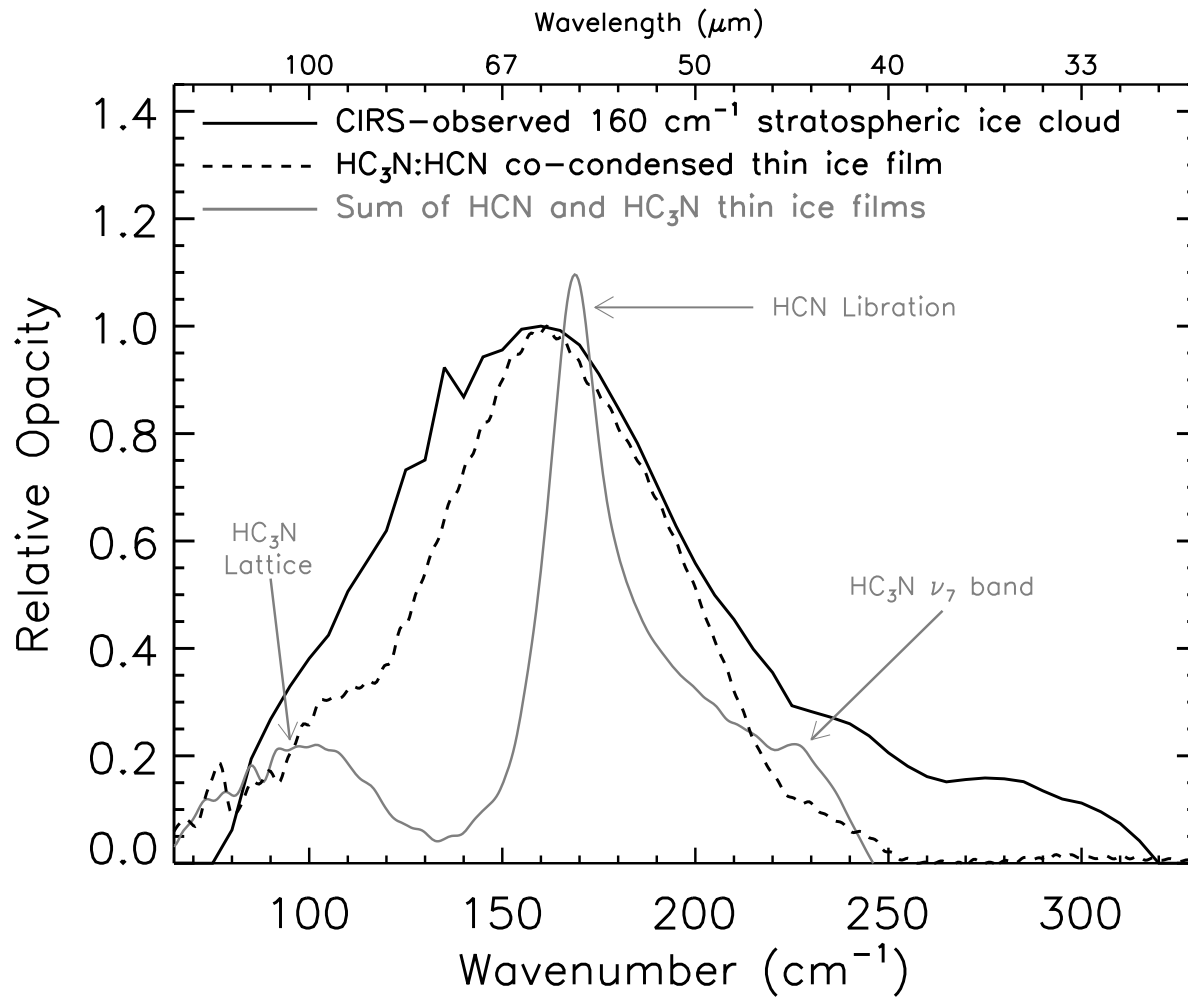
Figure 8. Modified from Anderson & Samuelson (2011). The solid black curve is the CIRS-derived spectral dependence of Titan's 160 cm^{-1} northern winter stratospheric ice cloud. The dashed black curve is a co-condensed thin ice film (vapors deposited at 30 K) for a 1.26:1 HC$_3$N:HCN ice mixture. The grey curve is the weighted sum of the individual ices of HCN and HC$_3$N (vapors deposited at 110 K) using the SPECTRAL chamber. This figure demonstrates that co-condensed ices, rather than the sum of their pure ice counterparts, better reproduce the spectral dependence of the CIRS-derived stratospheric ice cloud observations.
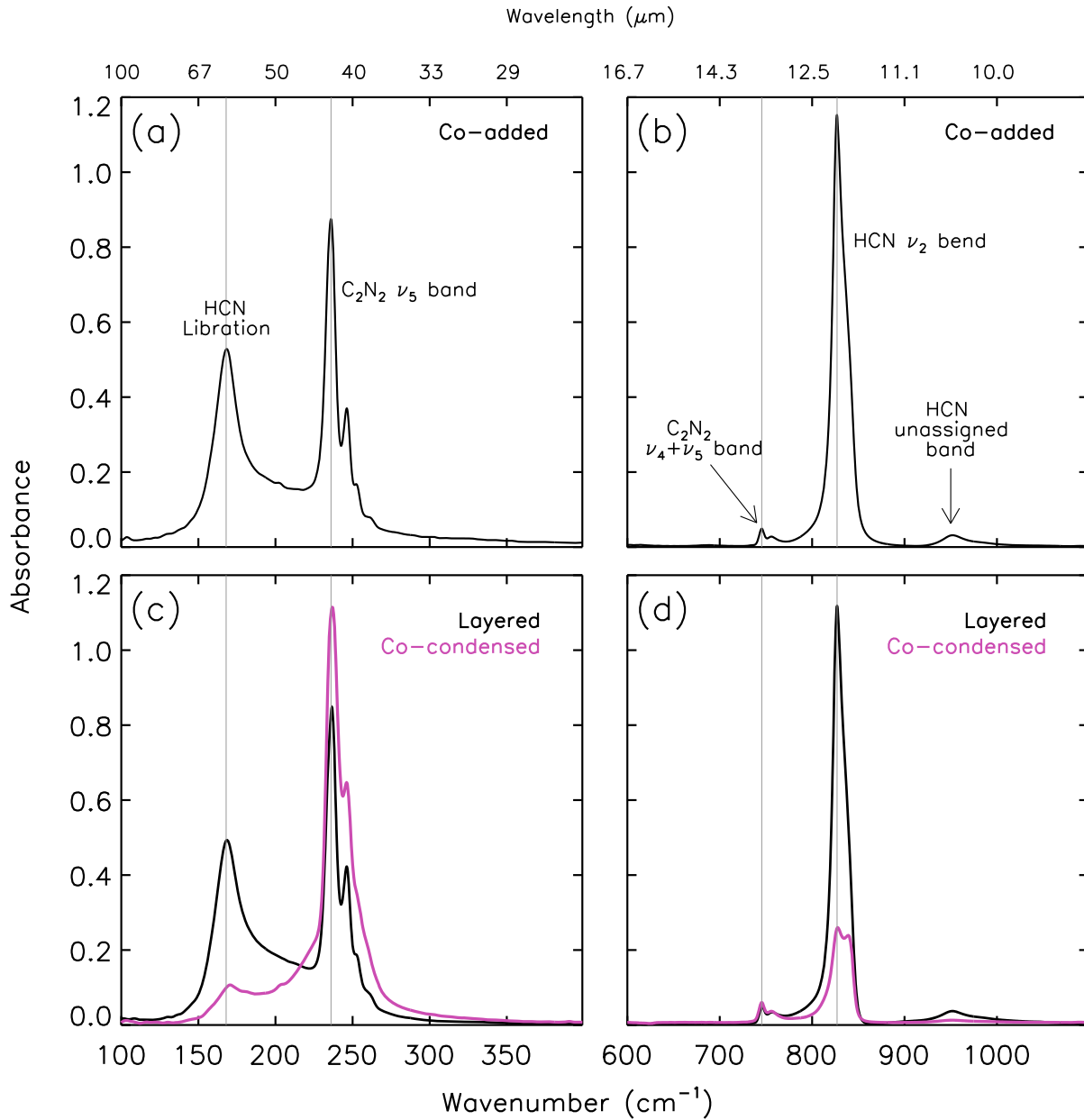
Figure 9. Absorbance spectra of various HCN ice and C_2N_2 ice combinations (all vapors were deposited at 110 K). The top row (panels a and b) shows the co-added absorbances of a 4.39-μm thick film of HCN ice (libration at 168 cm^{-1}; ν_2 bending mode at 827 cm^{-1}; unassigned band at 953 cm^{-1}) and a 4.25-μm thick film of C_2N_2 ice (ν_5 band has four peaks at 236 cm^{-1}, 246 cm^{-1}, 253 cm^{-1}, 262 cm^{-1}; $\nu_4 + \nu_5$ band has three peaks at 733 cm^{-1}, 745 cm^{-1}, 756 cm^{-1}). Both vapors were deposited separately, and the resulting HCN and C_2N_2 ice absorbances were then co-added to simulate an ice particle layering effect. The bottom row (panels c and d) shows the experimental results from a 8.65-μm thick layered ice (black solid curves) and a 8.33-μm thick co-condensed ice (pink solid curves). In the layered ice experiment, the bottom ice layer contains a 4.35-μm thick film of C_2N_2 and the top layer comprises a 4.31-μm thick film of HCN. In the co-condensed experiment, HCN and C_2N_2 vapors were mixed in a 1:1 ratio, then co-deposited. As expected, the spectral dependence of layered C_2N_2 and HCN ice is very similar to that of the co-added ices. On the other hand, neither the spectral appearance of the co-added ice nor the layered ice experiments reproduce those of the co-deposition experiments.
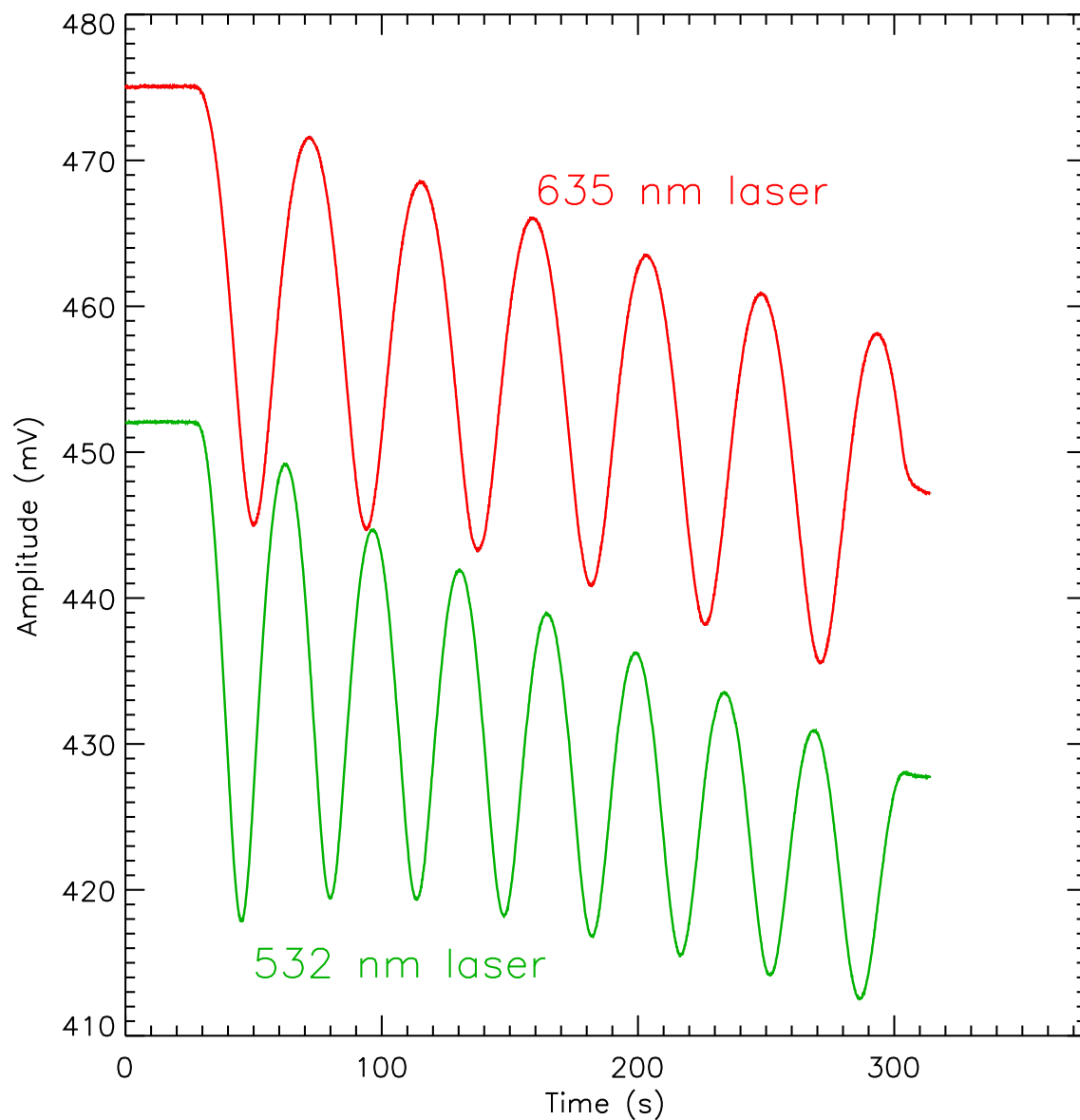
Figure 10. Amplitude vs. Time dependence of the 635-nm (top red curve) and the 532-nm (bottom green curve) laser interference fringe patterns. These curves are the result of constructive and destructive interferences arising from the reflected layers of a 1.90-μm thick film of HCN ice (vapor deposited at 110 K) as it grows with time.
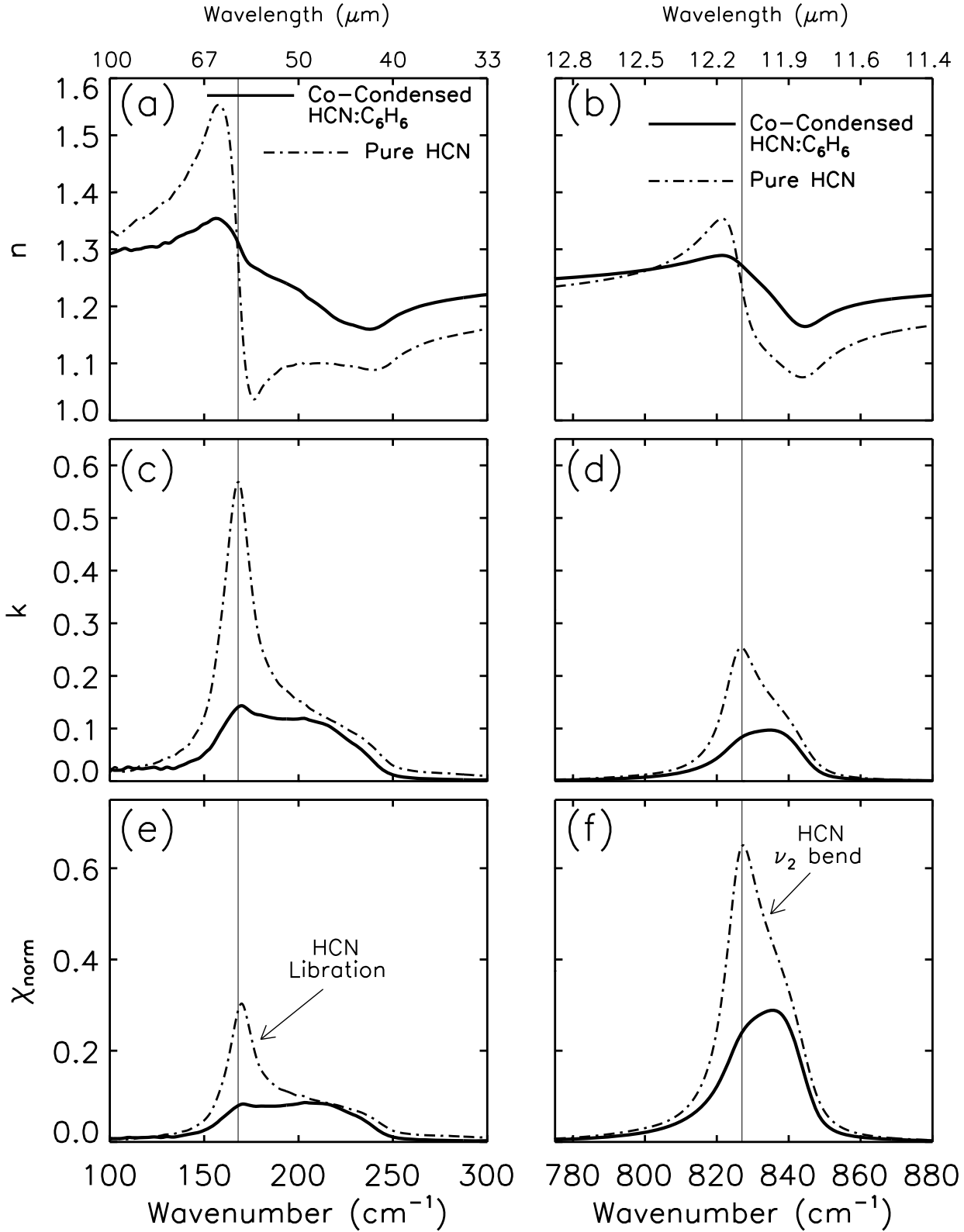
Figure 11. Refractive indices (real part n – panels a and b; imaginary part k – panels c and d) and normalized ice particle extinction cross sections χ_{norm} (panels e and f) for both the libration and ν_2 bending modes of a 4.39-μm thick film of pure HCN ice (dash-dot curves) and a 4.29-μm thick film of an HCN:C$_6$H$_6$ co-condensed ice containing 39% HCN and 61% C$_6$H$_6$ (solid curves); all vapors were deposited at 110 K. The thin vertical lines are located at 168 cm^{-1} and 827 cm^{-1}, which are the peak wavenumbers in k for the libration and ν_2 bend of pure HCN ice. The large asymmetry in the real part of the refractive index for pure HCN causes the effective particle cross section peak to shift to lower wavenumbers, which is not observed for the co-condensed ice since the real part of the refractive index for the HCN:C$_6$H$_6$ mixture is more symmetric, causing the effective particle cross section peak to remain relatively un-shifted in wavenumber. The imaginary part of the refractive index also contributes to the change in the effective particle cross section by shifting the wavenumber peak of the co-condensed ice to higher wavenumbers.